Appl Phys A (2011) 102: 713–717
DOI 10.1007/s00339-010-5965-9

Applied Physics A
Materials Science & Processing

Effects of ion-doping at different sites on multiferroic properties of $BiFeO_3$ thin films

Jun Liu · Meiya Li · Zhongqiang Hu · Ling Pei · Jing Wang · Xiaolian Liu · Xingzhong Zhao

Received: 4 March 2010 / Accepted: 5 July 2010 / Published online: 4 August 2010

Abstract A-site Ce and B-site Zr codoped $Bi_{1-x}Ce_xFe_{1-y}Zr_yO_3$ (BCFZ) thin films with different compositions were successfully prepared on the $Pt/Ti/SiO_2/Si$ substrates by chemical solution deposition. The influence of the A-site Ce and B-site Zr codoping on the structure, surface morphology, electrical and magnetic properties of BFO films were investigated, respectively. The comparative study suggested that the A-site Ce doping with various contents have notable influences on the electrical properties of the BFO films, while the B-site Zr doping with different contents affect mainly the magnetic properties of the BFO films. Compared with the other BCFZ films studied here, the $Bi_{0.97}Ce_{0.03}Fe_{0.97}Zr_{0.03}O_3$ film showed the lowest dielectric loss and leakage current density, a well-squared P–E loop and fatigue-free characteristics as well as the strong magnetization.

1 Introduction

Multiferroic materials that show ferroelectric and ferromagnetic ordering simultaneously are currently attracting significant attention due to their interesting fundamental physics as well as the potential applications [1–5]. Among the single-phase multiferroic materials studied so far, $BiFeO_3$, with a rhombohedrally distorted perovskite structure with space group R3c, is the only one that exhibits both ferroelectricity and G-type antiferromagnetism at room temperature (with Curie temperature $T_c \sim 1103$ K and Néel temperature $T_N \sim 643$ K), which makes it most possible for applications at room temperature [6–8].

However, pure BFO has a serious high leakage current problem resulted from the charge defects such as oxygen vacancies and the cancellation of the ion magnetic moments due to its spatial periodic inhomogeneous spin structure [8, 9], which hindered its practical applications in multiferroic devices. To improve the properties of BFO, considerable efforts have been made, for instance, A-site substitution with La^{3+}, Nd^{3+}, Ce^{3+} and Tb^{3+} [10–15] and B-site substitution with Ni^{2+}, Cu^{2+}, Co^{2+}, Cr^{3+}, Mn^{3+}, Ti^{4+}, Zr^{4+} and V^{5+} [16–18] etc. These studies showed that the ion-doping is an effective method to improve the properties of BFO. Since the ferroelectricity and magnetism of BFO come respectively from the lone pair electrons of A-site Bi^{3+} ions and the antiferromagnetic ordering of B-site Fe^{3+} ions [3–5], the comparative study of the effects of ion-doping at A-site and B-site, respectively, on ferroelectric and ferromagnetic properties, is very important [15, 18]. However, few work related to this was reported. Recently, our study revealed that the A-site Ce and B-site Zr codoping could improve the ferroelectric and ferromagnetic properties of BFO films [19]. Therefore, in this paper, we prepared the A-site Ce and B-Site Zr codoped BFO films with different compositions on $Pt/Ti/SiO_2/Si$ substrates by chemical solution deposition (CSD) and investigated the influences of ion-doping at different sites on the microstructure and multiferroic properties of the BFO films.

J. Liu · M. Li (✉) · Z. Hu · L. Pei · J. Wang · X. Liu · X. Zhao
School of Physics and Technology, Wuhan University,
Wuhan 430072, P.R. China
e-mail: myli@whu.edu.cn
Fax: +86-27-68752569

J. Liu · M. Li · Z. Hu · L. Pei · J. Wang · X. Liu · X. Zhao
Key Laboratory of Artificial Micro- and Nano-structures
of the Ministry of Education, Wuhan University, Wuhan 430072,
P.R. China

2 Experiments

The precursor solutions used in CSD were prepared by dissolving bismuth nitrate [$Bi(NO_3)_3 \cdot 5H_2O$], iron nitrate [$Fe(NO_3)_3 \cdot 9H_2O$], cerium nitrate [$Ce(NO_3)_3 \cdot 9H_2O$] and zirconium nitrate [$Zr(NO_3)_4 \cdot 3H_2O$] in a mixed solution of acetic acid and 2-methoxyethanol to form the final products with nominal compositions of $BiFeO_3$ (BFO), $Bi_{1-x}Ce_xFe_{1-y}Zr_yO_3$ (BCFZ) ($x = 0.03$, $y = 0.03$; $x = 0.06$, $y = 0.03$; $x = 0.06$, $y = 0.06$; i.e. $Bi_{0.97}Ce_{0.03}Fe_{0.97}Zr_{0.03}O_3$ ($BCFZ_{33}$), $Bi_{0.94}Ce_{0.06}Fe_{0.97}Zr_{0.03}O_3$ ($BCFZ_{63}$), $Bi_{0.94}Ce_{0.06}Fe_{0.94}Zr_{0.06}O_3$ ($BCFZ_{66}$)). 5 mol% of excess Bi was added to compensate the bismuth loss during the heat treatment. The solutions were spin coated on the $Pt/Ti/SiO_2/Si$ substrates at 3500 rpm for 20 s and dried at 150°C for 5 min, and then pre-fired at 350°C for 10 min in air. This process was repeated several times to obtain the desired film thickness. The films were then annealed at 600°C for 10 min in an oxygen atmosphere for crystallization. To measure the electrical properties of the films, circular Pt electrodes with diameter of 0.2 mm were fabricated on the surface of the films by rf-magnetron sputtering.

The structure of the films was analyzed by an x-ray diffractometer (D8 Advance, Bruker, German) with CuK_α radiation. The surface morphology was observed by an atomic force microscope (AFM, SPM-9500J3). The dielectric constants and losses of these films were measured using an Agilent 4294A precision impedance analyzer. The leakage current, ferroelectric properties, and anti-fatigue properties of these films were measured by a ferroelectric test system (Precision Premier Workstation, Radiant Technology, USA). The magnetic properties of these films were measured by a physical property measurement system (PPMS, USA). All of these measurements were carried out at room temperature.

3 Results and discussion

Figure 1 shows the XRD patterns of the BCFZ films. All the films show single-phase polycrystalline perovskite structure except a trace of unknown impurity observed in the $BCFZ_{66}$ film. To further investigate the influence of Ce and Zr doping on the structure of the films, the subtle XRD patterns in the 2θ range of 31.5°–32.5° are given. As seen in the inset of Fig. 1, two clearly separated reflection peaks of (104) and (110) in the vicinity of $2\theta = 32°$ in the pattern of the pure BFO film are merged into a single peak in the patterns of the Ce and Zr codoped BCFZ films, which suggests a structure transition from the rhombohedral to the pseudotetragonal [10, 12, 16]. This is in accordance with our previous reports [14, 19]. In addition, with the increase of Ce doping, this single peak in the pattern of the $BCFZ_{33}$ film has a tendency to shift towards higher 2θ angle as observed in that of

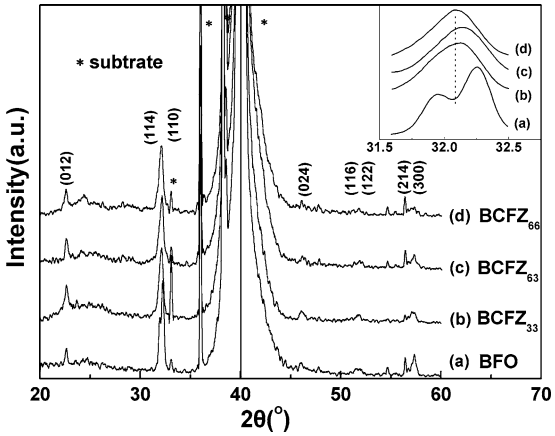

Fig. 1 XRD patterns of the BCFZ thin films, where *the inset* shows the magnified patterns in the vicinity of $2\theta = 32°$

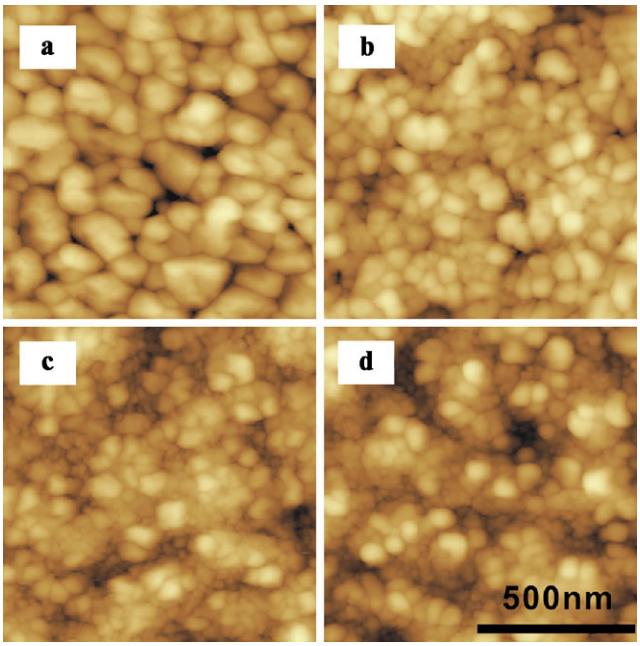

Fig. 2 AFM images of the films of (**a**) BFO, (**b**) $BCFZ_{33}$, (**c**) $BCFZ_{63}$ and (**d**) $BCFZ_{66}$

the $BCFZ_{63}$ film, while with the increase of Zr doping, the corresponding single peak in the pattern of the $BCFZ_{63}$ film has a tendency to shift towards lower 2θ angle as shown in that of the $BCFZ_{66}$ film, which indicate lattice distortion of these films. This may be mainly attributed to the fact that the ionic radii of A-site Ce ions (Ce^{3+} (0.101 nm), Ce^{4+} (0.087 nm)) is smaller than that of Bi^{3+} (0.103 nm) but the ionic radius of B-site Zr^{4+} (0.072 nm) is larger than that of Fe^{3+} (0.064 nm) [20].

Figure 2 presents the surface morphology of the BCFZ films using an atomic force microscope (AFM). The pure BFO film has large grain size with a few interstices, while the $BCFZ_{33}$ film possesses denser surface and smaller

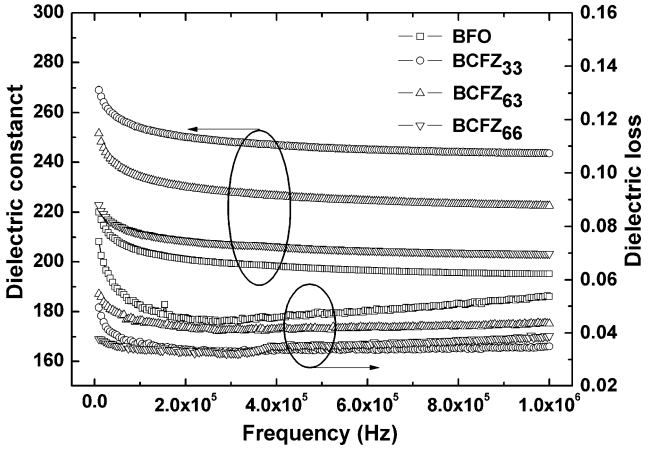

Fig. 3 The ε_r and $\tan\delta$ of the BCFZ films varied with frequencies

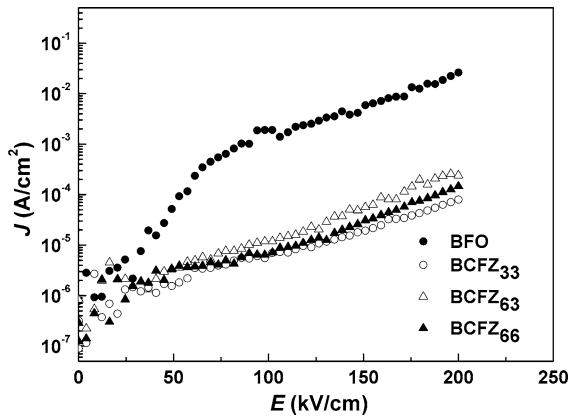

Fig. 4 Leakage current density (J) versus electric field (E) for the BCFZ films

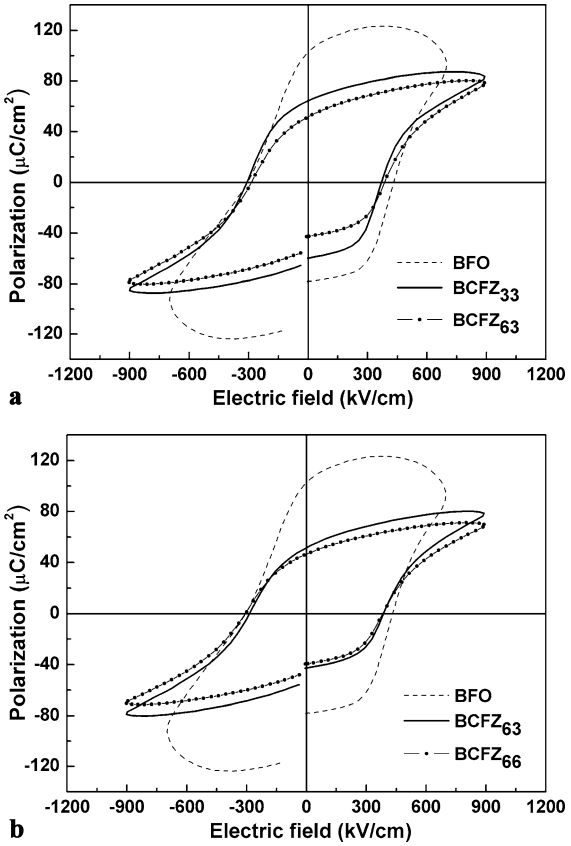

Fig. 5 P–E loops of the BCFZ films of (**a**) BFO, $BCFZ_{33}$ and $BCFZ_{63}$; (**b**) BFO, $BCFZ_{63}$ and $BCFZ_{66}$

grains. With the increase of Ce content, the grain size of $BCFZ_{63}$ film decreases further, revealing that the A-site Ce doping reduces significantly the grain size of the BFO films. While compared with $BCFZ_{63}$ film, the grain size of $BCFZ_{66}$ film have no obvious change with the increase of Zr content, indicating that the B-site Zr doping has little influence on the grain size of the BFO films.

Figure 3 illustrates the frequency dependence of the dielectric constant (ε_r) and loss tangent ($\tan\delta$) of the BCFZ thin films. The frequency dependence of the ε_r values of all the films show similar features in the measured frequency range. Compared with the pure BFO film, the Ce and Zr codoped BCFZ films have much larger ε_r values and much smaller $\tan\delta$ values. And among them, the $BCFZ_{33}$ film possesses the largest ε_r and smallest $\tan\delta$ values.

Figure 4 exhibits the dependence of the leakage current density (J) of the BCFZ films on the applied electric field (E). As shown in the figure, the BFO film exhibits a relatively high leakage current density, while the Ce and Zr codoped BCFZ films have lower leakage current densities. Under an applied electric field of 150 kV/cm, the leakage current densities of the $BCFZ_{33}$, $BCFZ_{63}$ and $BCFZ_{66}$ films are about 7.99×10^{-5} A/cm^2, 2.41×10^{-4} A/cm^2 and 1.47×10^{-4} A/cm^2, respectively. Among them, the $BCFZ_{33}$ film shows the lowest leakage current density, which is consistent with the smallest dielectric losses of the sample discussed above. Meantime, the reducing amount of the leakage current density of $BCFZ_{33}$ film relative to $BCFZ_{63}$ film is larger than that of $BCFZ_{66}$ film to it. This suggests that the A-site Ce doping is more effective in reducing the leakage current density of BFO film than the B-site Zr doping.

The ferroelectric hysteresis loops (P–E loops) of the BCFZ films are presented in Fig. 5. The pure BFO film exhibits a poor P–E loop evidenced by the rounded drop-down tips and the large relaxation gap, which shows significant influence of the space charges such as oxygen vacancy on the P–E loop [21, 22]. However, the Ce and Zr codoped BCFZ films exhibit good P–E loops without obvious features of leakage current. Meanwhile, as shown in Fig. 5(a), the $BCFZ_{33}$ film has a better square-shaped P–E loop with a larger remnant polarization than that of $BCFZ_{63}$ film. While with the increase of Zr content, the $BCFZ_{63}$ and $BCFZ_{66}$ films show no much difference in remanent polarization and the shape of P–E loops. These illuminate that the $BCFZ_{33}$ film shows the best P–E loop of all the films

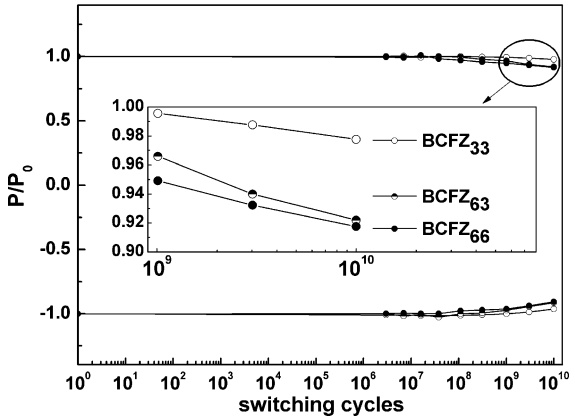

Fig. 6 Fatigue measurement of the BCFZ films

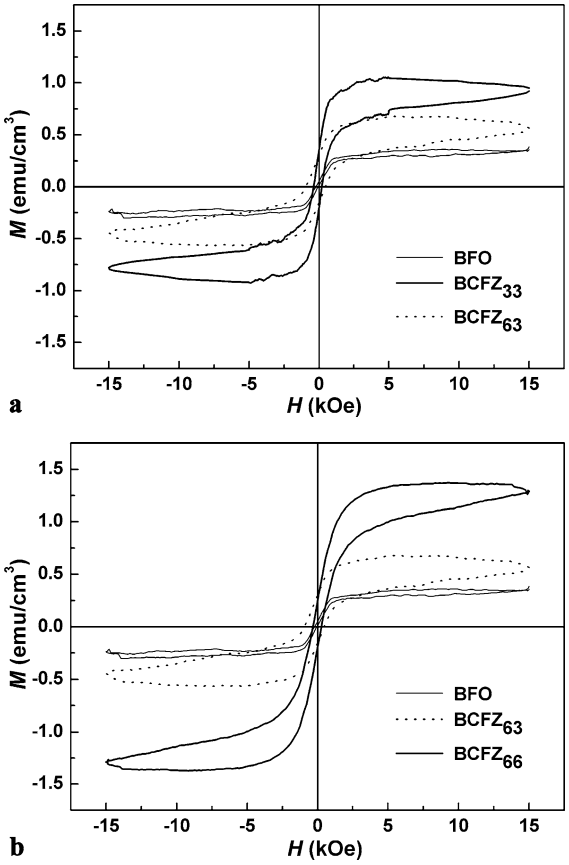

Fig. 7 M–H hysteresis loops of the films of (**a**) BFO, $BCFZ_{33}$ and $BCFZ_{63}$; (**b**) BFO, $BCFZ_{63}$ and $BCFZ_{66}$

and the A-site and B-site doping have different effects on the ferroelectric properties of BFO films. For the BFO material, the ferroelectricity comes mainly from the lone $6s^2$ pair of electrons in the A-site Bi ions, which hybridize with an empty p orbit of oxygen ions [3–5]. In addition, from the result of leakage current discussed above, the A-site Ce doping can effectively reduce the leakage current, which may helpful to manifest the intrinsic ferroelectric property [21, 22]. Thereby, it is more efficient to improve the ferroelectric properties of BFO films by the A-site Ce doping than the B-site Zr doping.

Fatigue behavior of the BCFZ films at a measuring frequency of 1 MHz is depicted in Fig. 6, in which the inset shows the enlarged fatigue curves for the films after being subjected to $10^9 \sim 10^{10}$ switching cycles. The anti-fatigue curves of the pure BFO film was not obtained because of the high leakage current density of the film. As seen in the inset of Fig. 6, after being subjected to 1×10^{10} switching cycles, the remanent polarization of the $BCFZ_{63}$ and $BCFZ_{66}$ films decreased by 8% and 9% respectively, while that of the $BCFZ_{33}$ film dropped by only 2%, showing the best anti-fatigue property. Compared the anti-fatigue properties of the $BCFZ_{33}$ film with that of the $BCFZ_{63}$ film and the $BCFZ_{63}$ film with the $BCFZ_{66}$ film, respectively, it can be found that the anti-fatigue properties of these films varied much larger with the content of the A-site Ce doping than that of the B-site Zr doping. It is believed that the physical origin of the polarization fatigue is the domain wall pinned by the space charge such as oxygen vacancies [21]. As was discussed above, the leakage current density of the films decreased more by the A-site Ce doping due to the eliminating of oxygen vacancies than by the B-site Zr doping. Therefore, the A-site Ce doping could also reduce the pinned domain walls by the reducing of oxygen vacancies, and thus enhance the anti-fatigue resistance of BFO films.

The magnetic hysteresis (M–H) loops of the BCFZ films are measured using a PPMS with the magnetic field applied parallel to the film surface, as shown in Fig. 7. All the films demonstrate a weak ferromagnetic behavior and the magnetizations of all the Ce and Zr codoped BCFZ films are stronger than that of the pure BFO film. Under an applied magnetic field of 15 kOe, the $BCFZ_{66}$ film demonstrates the strongest magnetization with a saturation magnetization (M_s) of 1.3 emu/cm^3 and the $BCFZ_{33}$ film also shows a well ferromagnetic behavior with a saturation magnetization (M_s) of 1.0 emu/cm^3. The enhancement of magnetization in BFO-based materials is usually attributed to either the destroying of the spatially inhomogeneous spin-modulated incommensurate structure to release weak ferromagnetism, or the increasing of the spin canting angle resulting in the net macroscopic magnetization [8, 10]. Noting that the structure transition was observed in all the Ce and Zr codoped films, as mentioned in the XRD analysis above, the structure transition may therefore be the main cause for the increase of the magnetization in the BCFZ films. By comparing Fig. 7(a) with Fig. 7(b), the A-site Ce doping shows a weaker influence on the magnetization of BFO films than the B-site Zr doping. The cause for the increase of magnetization in the doped BFO films could also be the formation of Fe^{2+} ions which would possible generate a double exchange interaction with Fe^{3+} ions through the oxygen ions [10, 23]. The high-valence Zr^{4+} substitution for the Fe^{3+} at

the B-site may bring in more Fe^{2+} ions due to the charge compensation and consequently enhance the magnetization of BFO films [16, 19, 23]. Therefore, the B-site Zr doping could improve the magnetic properties of BFO films more effectively than the A-site Ce doping due to the formation of Fe^{2+} ions.

4 Conclusions

In summary, the A-site Ce and B-site Zr codoped BCFZ films with different compositions were successfully prepared on the Pt/Ti/SiO_2/Si substrates by chemical solution deposition. Among these films studied, the $Bi_{0.97}Ce_{0.03}Fe_{0.97}Zr_{0.03}O_3$ film showed the lowest dielectric loss and leakage current density, a well-squared P–E loop and the fatigue-free characteristics as well as the strong magnetization. Meanwhile, the comparative study suggested that the A-site Ce doping with various contents have notable influences on the electrical properties including the leakage current, ferroelectric properties and anti-fatigue resistance of the BFO films. This may be related to the modification of the structure and the elimination of charge defects due to the A-site Ce doping. In contrast, the B-site Zr doping with different content affect mainly the magnetic properties of the BFO films, which may be ascribed to the structure transition and the possible increase of Fe^{2+} ions resulted from the high-valence Zr substitution.

Acknowledgement This work was supported by the National Natural Science Foundation of China (Grant No. 50872097).

References

1. J. Wang, J.B. Neaton, H. Zheng, V. Nagarajan, S.B. Ogale, B. Liu, D. Viehland, V. Vaithyanathan, D.G. Schlom, U.V. Waghmare, N.A. Spaldin, K.M. Wuttig, R. Ramesh, Science **299**, 1718 (2003)
2. W. Eerenstein, F.D. Morrison, J. Dho, M.G. Blamire, J.F. Scott, N.D. Mathur, Science **307**, 1203 (2005)
3. L.W. Martin, S.P. Crane, Y.H. Chu, M.B. Holcomb, M. Gajek, M. Huijben, C.H. Yang, N. Balke, R. Ramesh, J. Phys. C, Condens. Matter **20**, 434220 (2008)
4. G. Catalan, J.F. Scott, Adv. Mater **21**, 2463 (2009)
5. K.F. Wang, J.M. Liu, Z.F. Ren, Adv. Phys. **58**, 321 (2009)
6. G.A. Smolenskii, I.E. Chupis, Sov. Phys. Usp. **25**, 475 (1982)
7. I. Sosnowska, T. Peterlin-Neumaier, E. Steichele, J. Phys. C, Condens. Matter **15**, 4835 (1982)
8. C. Ederer, N.A. Spaldin, Phys. Rev. B **71**, 060401 (2005)
9. X.D. Qi, J. Dho, R. Tomov, M.G. Blamire, J.L. MacManus-Driscoll, Appl. Phys. Lett. **86**, 062903 (2005)
10. F.Z. Huang, X.M. Lu, W.W. Lin, X.M. Wu, Y. Kan, J.S. Zhu, Appl. Phys. Lett. **89**, 242914 (2006)
11. B.F. Yu, M.Y. Li, J. Liu, D.Y. Guo, L. Pei, X.Z. Zhao, J. Phys. D, Appl. Phys. **41**, 065003 (2008)
12. Y. Wang, C.W. Nan, J. Appl. Phys. **103**, 024103 (2008)
13. J. Liu, M.Y. Li, L. Pei, B.F. Yu, D.Y. Guo, X.Z. Zhao, J. Phys. D, Appl. Phys. **42**, 115409 (2009)
14. J. Liu, M.Y. Li, L. Pei, J. Wang, B.F. Yu, X. Wang, X.Z. Zhao, J. Alloys Compd. **493**, 544 (2010)
15. A. Lahmar, S. Habouti, M. Dietze, C.-H. Solterbeck, M. Es-Souni, Appl. Phys. Lett. **94**, 012903 (2009)
16. Y. Wang, C.W. Nan, Ferroelectrics **357**, 172 (2007)
17. H. Naganuma, J. Miura, S. Okamura, Appl. Phys. Lett. **93**, 052901 (2008)
18. P. Kharel, S. Talebi, B. Ramachandran, A. Dixit, V.M. Naik, M.B. Sahana, C. Sudakar, R. Naik, M.S.R. Rao, G. Lawes, J. Phys. C, Condens. Matter **21**, 036001 (2009)
19. J. Liu, M.Y. Li, L. Pei, J. Wang, Z.Q. Hu, X. Wang, X.Z. Zhao, Europhys. Lett. **89**, 57004 (2010)
20. R.D. Shannon, Acta Crystallogr. A **32**, 751 (1976)
21. Z.X. Cheng, X.L. Wang, S.X. Dou, Phys. Rev. B **77**, 092101 (2008)
22. W. Eerenstein, F.D. Morrison, F. Sher, J.L. Prieto, J.P. Attfield, J.F. Scott, N.D. Mathur, Philos. Mag. Lett. **87**, 249 (2007)
23. Z.Q. Hu, M.Y. Li, B.F. Yu, L. Pei, J. Liu, J. Wang, X.Z. Zhao, J. Phys. D, Appl. Phys. **42**, 185010 (2009)